Fabrication of Stochastic Ni@PVP Nanowire Networks for Memristive Platforms

Catarina Lemos , Catarina Dias , Rui S. Costa * , João Ventura

Posted Date: 4 March 2026

doi: 10.20944/preprints202603.0293.v1

Keywords: electrochemical metallization; memristors; neuromorphic hardware; nickel nanowires; resistive switching

 doi:10.20944/preprints202603.0293.v1

Article

Fabrication of Stochastic Ni@PVP Nanowire Networks for Memristive Platforms

Catarina Lemos, Catarina Dias, Rui S. Costa * and João Ventura

IFIMUP, Departamento de Física e Astronomia, Faculdade de Ciências, Universidade do Porto, Rua do Campo Alegre s/n, 4169-007 Porto, Portugal

* Correspondence: rucosta@fc.up.pt

Abstract

Single memristive nanowire networks have emerged as a promising pathway for energy-efficient neuromorphic computing, owing to their intrinsic nonlinearity, high dimensionality, fading memory and volatile switching dynamics relevant to physical reservoir computing. While prior works focused on oxide or silver-based network systems, these approaches face trade-offs between operating voltage, cost, stability, and scalability. This work presents a proof-of-concept demonstration of stochastic polyvinylpyrrolidone (PVP)-coated nickel nanowire networks as low-cost and scalable memristive platform, exhibiting low-voltage resistive switching (1–2 V). The electrical characterization reveals predominantly volatile resistive switching combined with nonvolatile behavior, consistent with a filamentary conduction mechanism at nanowire junctions. The switching dynamics are governed by the polymer coating thick-ness, with intermediate PVP concentration (Ni@PVP = 1:25) showing optimal performance, with a resistance ratio of ~ 200, stable retention over 1 h, and a reproducible endurance of over 45 cycles. These results establish Ni@PVP nanowire networks as promising memristive platforms for neuromorphic hardware applications and physical reservoir computing, with relevant properties such as fading memory and nonlinear dynamics.

Keywords: electrochemical metallization; memristors; neuromorphic hardware; nickel nanowires; resistive switching

1. Introduction

Neuromorphic computing has emerged as a promising alternative to conventional von Neumann architectures, where the physical separation between memory and processing units leads to massive power consumption in large-scale systems [1,2]. Neuromorphic systems shift the computational paradigm by drawing inspiration from the brain, which performs ~10^{16} operations per second while consuming only 20 W [3]. By emulating the structure and functionality of biological neurons and synapses, neuromorphic networks enable highly parallel and low-power computation [4].

Among neuromorphic paradigms, reservoir computing (RC) provides an efficient framework that can significantly reduce training and computational costs. In RC, a fixed nonlinear dynamical system, known as the reservoir, transforms inputs into a high dimensional representation, while only a linear read-out layer is trained to produce the output [5]. Interestingly, any physical system that exhibits nonlinearity, high dimensionality, fading memory and separation property can serve as a reservoir [6].

Within this context, memristive devices have gathered interest as artificial synapses for reservoirs due to their scalability, low-power operation and simple structure [7,8]. Among RC architectures [9], self-assembled nanowire (NW) networks stand out due to their strong morphological and topological similarity to biological neuronal networks, exhibiting small-world connectivity, nonlinearity, separation property, fading memory, and high dimensionality [10]. Their

 doi:10.20944/preprints202603.0293.v1

neuromorphic behavior arises from filamentary resistive switching (RS) at NW junctions that act as artificial synapses. An insulating polymeric or oxide-based shell [11] enables the formation and rupture of conductive filaments, inducing SET transitions from a high-resistance state (HRS, R_{OFF}) to a low-resistance state (LRS, R_{ON}), and RESET in the reverse direction. The intrinsic stochastic morphology of the network leads to the formation of many junctions, resulting in rich high dimensional and nonlinear dynamics.

To date, most memristive NW networks reported for physical RC rely on oxide-based systems [12,13], noble metals such as silver [14–17], and organic/organic nanowires like single-walled carbon nanotube (SWNT)/polyoxometalate (POM), SWNT/porphyrinpolyoxometalate (Por-POM), and SWNT/liquid crystals [18]. Oxide-based networks, such as Ni/NiO [13,19,20] and Cu/CuO core-shell NWs [14], show high R_{OFF}/R_{ON} but require high SET voltages (>5 V) and rely on ordered structures [19,21]. In contrast, Ag-based NW networks, particularly Ag/polyvinylpyrrolidone (PVP) enable low-voltage RS in fully stochastic self-assembled architectures [16,17,22]. For instance, Milano et al. demonstrated in-materia RC capable of temporal data processing, highlighting the potential of stochastic memristive systems as physical reservoirs [17,22]. However, Ag-based devices suffer from high cost, limited long-term stability, and scalability issues, motivating the search for alternative materials. Nickel emerges as a promising candidate due to its abundance, chemical stability, and compatibility with scalable chemical synthesis methods. Previous studies focused on ordered Ni/NiO core-shell NW networks, reporting SET values of 6–8 V in crossbar arrays [19] and similar behavior in magnetically aligned NW meshes [20]. Among polymer coatings, PVP is especially attractive, as it enables ionic transport and filament formation at NW junctions, leading to RS in metal NW networks [16,22].

In this work, we present a study of stochastic networks of PVP-coated nickel (Ni@PVP) NWs. Through comprehensive structural and morphological characterization using X-ray diffraction, Raman spectroscopy and Scanning Electron Microscopy, combined with electrical analysis of switching behavior, volatility, retention, and endurance, we demonstrate that Ni@PVP achieve competitive memristive performance, with low switching voltages (1–2 V) and R_{OFF}/R_{ON}~200. These findings establish Ni@PVP NW networks as a promising cost-effective and scalable platform for neuromorphic hardware implementations.

2. Materials and Methods

2.1. Synthesis of Ni NWs

Ni NWs were synthesized via a magnetically assisted simple chemical reduction method in a polyol medium [23,24]. Typically, 0.150 g of PVP (MW=40,000 g mol^{-1} from Sigma-Aldrich) was dissolved in 30 mL of ethylene glycol (EG, 99% from Carlo Erba Reagents) followed by the dissolution of 0.036 g of nickel (II) chloride hexahydrate ($NiCl_2 \cdot 6H_2O$, 98% from Sigma-Aldrich) in the same flask. After complete dissolution, 1 mL of hydrazine monohydrate (>98%, from Alfa Aesar) was added dropwise. The reaction was then placed in a pre-heated oil bath maintained at 85 °C, above a magnet for 30 min. Approximately 5 min later, a black precipitate began to form at the surface. At the end, the product was collected with a magnet and washed three times with ethanol to remove unreacted precursors. The obtained material was redispersed and stored in 10 mL of pure ethanol (>99%).

2.2. Fabrication of Ni NW Network

The fabricated single-coated Ni@PVP NWs were subsequently double-coated with PVP. This was achieved by dispersing the Ni NWs in freshly prepared PVP solutions dissolved in pure ethanol, with different Ni:PVP weight ratios (1:10, 1:25, 1:50), using a mechanical stirrer at 200 rpm for 6 h at room temperature. The resulting samples are referred as Ni@PVP_{SC}, Ni@$PVP_{1:10}$, Ni@$PVP_{1:25}$, and Ni@$PVP_{1:50}$ NWs.

Ion beam deposition was used to fabricate Al (150 nm)/W (75 nm) thin films on glass substrates in a working pressure of 1.4×10^{-4} Torr (5 sccm of Ar flux; base pressure below 10^{-6} Torr). An array of

 doi:10.20944/preprints202603.0293.v1

two 30 μm wide electrodes separated by a 100 μm gap were then defined by photolithography. The photoresist (Microposit S1818 G2 photoresist from Atis S. A) was spin-coated (2500 rpm, 35 s), pre-baked at 120 °C for 90 s, and exposed to UV light (365 nm, 48 s). Development was performed with a Microposit 351 developer. Finally, memristive nanowire networks were fabricated by depositing the Ni NWs dispersed in pure ethanol at the electrode gaps by drop casting 4–5 drops (8 μL).

2.3. NWs and Network Characterization

The morphology of the NWs was characterized using scanning electron microscopy (SEM) with a high-resolution scanning microscope FEI Quanta 400 FEG ESEM using a 15 kV in both scattering and backscattering electrons mode. Structural analysis was performed using X-ray diffraction (XRD) with a SmartLab Rigaku diffractometer using Cu K_α radiation (λ = 1.5404 Å) in the Bragg-Brentano $\theta/2\theta$ configuration with a range of 10° to 90°, with a step of 0.01°. Composition was obtained using Raman spectra at room temperature with a Renishaw inVia Qontor Spectrometer in the 200–3500 cm^{-1} spectral range using a 532 nm edge He-Ne laser line at 1.7 mW and a 50× magnification lens, with 20 s of exposure and 1% power for 3 accumulations. The electrical behavior of the networks was characterized at room temperature using two tungsten microprobes and a 2410 Keithley SourceMeter, applying voltage cycles from 0 V → $+V_{max}$ → 0 V → $-V_{max}$ → 0 V. Retention measurements were performed for over 1 h by applying low voltage read pulses (3–5 mV) under a current compliance of 0.1–1 mA. Endurance was determined through repeated pulsed switching (+5 V and -1 V).

3. Results

3.1. Structure Characterization

To investigate the influence of polymer coating concentration on RS, the fabricated Ni NWs were double-coated at different Ni:PVP weight ratios (1:10, 1:25, and 1:50). SEM confirmed the formation of well-defined Ni NWs (Figure 1a), with single-coated NWs with an average diameter of 209 ± 26 nm and length of 23 ± 14 μm ranging from 5 to 85 μm. These dimensions are consistent across the different ratios of double-coating (Figure S1). The $Ni@PVP_{1:10}$ NWs exhibit a characteristic spiky surface (Figure 1b) and a surrounding coating layer. In secondary electrons image, these shapes appear as arrow-like protrusions (Figure 1c), while, in comparison, the corresponding backscattered electrons image (Figure 1d) reveals triangular structures extending from the NW surface. This indicates that the arrow-like shapes in secondary mode arises from imaging distortions associated with polymer coating layer rather than from the metallic NW surface itself, proving the successful coating [25]. No significant morphological differences were observed between the NWs prepared with and without double-coating process at different PVP ratios (Figure S2). In all cases, the NWs form a highly interconnected stochastic network with multiple junctions, revealing that the network architecture is preserved after the double-coating process.

 doi:10.20944/preprints202603.0293.v1

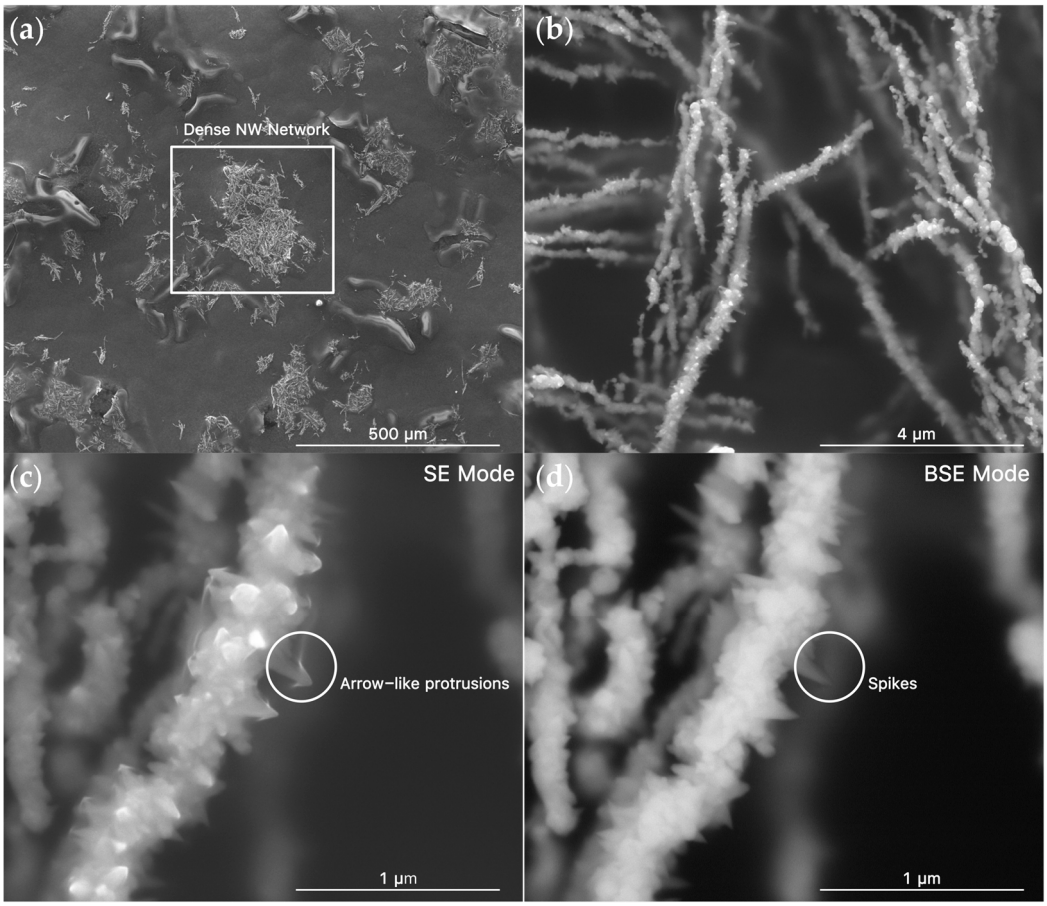

Figure 1. SEM images of Ni@PVP$_{1:10}$ at **(a)** low (200×) and **(b)** high (25 000×) magnifications for a dense NW network. SEM image of the surface of a single NW at a magnification of 100 000× for **(c)** secondary and **(d)** backscattered electron modes.

Figure 2a shows the XRD diffractograms of Ni@PVP$_{SC}$ and Ni@PVP$_{1:50}$ NWs, confirming the presence of metallic Ni through peaks at 45°, 52° and 76° corresponding to the (111), (200), and (220) planes of the face-centered cubic (FCC) crystal structure, respectively (JCPDS card 00-04-0850) [26,27]. For the highest PVP concentration (1:50), the additional broad peak at 20° is attributed to amorphous PVP resulting from increased polymer content [28,29].

Figure 2b shows the Raman spectra of single- and double-coated Ni NWs. Vibrational bands at 2928, 1660, 1495, 1464, 1448, 1426 and 1376 cm^{-1} are consistent with pure PVP [27], and their intensity increases with polymer content. Notably, the band at 2928 cm^{-1} corresponds to the asymmetric CH_2 stretching in the PVP backbone, indicating proximity of the polymer chain to the Ni NW surface [30]. The strong peak at ~1600 cm^{-1} is assigned to the PVP C=O stretch, while the vibrational bands between 1370–1500 cm^{-1} arise from CH_2/CH_3 deformation modes and PVP ring/C–N skeletal vibrations [31]. Together with XRD, these results confirm the presence of PVP and show that higher polymer content enhances the amorphous contribution, supporting the interpretation that the low-contrast surrounding layer observed in SEM images corresponds to the polymer coating.

 doi:10.20944/preprints202603.0293.v1

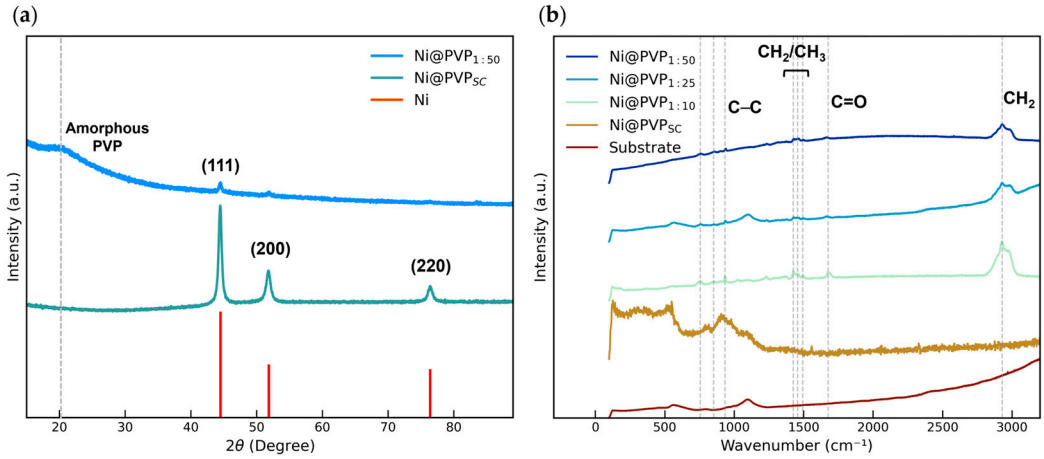

Figure 2. (a) XRD diffractograms of Ni@PVP$_{SC}$ and Ni@PVP$_{1:50}$. Ni and amorphous PVP peaks are highlighted with vertical lines. **(b)** Raman spectra of Ni NWs coated with different concentrations of PVP (single-coated, 1:10, 1:25, 1:50). PVP modes are highlighted with vertical lines.

3.2. Electrical Characterization

To assess the electrical properties of the Ni@PVP NWs, stochastic networks were drop-casted in between Al/W electrodes (Figure 3a). The Ni@PVP$_{SC}$ device shows linear ohmic behavior (Figure S3), confirming that a single synthesis-derived PVP layer provides insufficient NWs insulation to support RS. The double-coating Ni@PVP$_{1:25}$ and Ni@PVP$_{1:50}$ devices exhibited both nonvolatile and volatile RS. This coexistence reflects the inherent stochastic nature of the network architecture, where local variations in NW junction geometries and polymer thickness produce distinct switching behaviors across different current pathways. A representative nonvolatile *I–V* characteristic curve for Ni@PVP$_{1:25}$ is shown in Figure 3b. Initially, the network is in an HRS with a resistance of 1.4×10^3 Ω. Upon increasing the applied voltage up to +1.5 V, a SET occurs switching it to a LRS of 674 Ω. When the voltage is reduced and swept through zero bias, the LRS is retained, demonstrating nonvolatile behavior. During the reversed polarity voltage sweep, the electrical resistance switches back to HRS (RESET) at -1.1 V.

Under the same procedure, the Ni@PVP$_{1:25}$ network also exhibits a volatile RS behavior (Figure 3b). Upon increasing the voltage, the network shows a progressive increase in current and transitions to LRS of 230 Ω at around 1.2 V. As the applied voltage approaches zero, the device spontaneously relaxes back to the HRS of 5.2×10^3 Ω at around 0.2 V (volatile behavior). This indicates the formation of unstable conductive filaments that are only sustained under an applied electric field and dissolve with low voltages, likely due to ionic diffusion of the metal ions within the polymer layer. A similar volatile response is observed under negative polarity. Interestingly, the same NW network can exhibit nonvolatile switching during the first cycles before evolving into a dominant volatile regime. This suggests that, although conductive filaments can initially stabilize with the trappings of ions, continuing cycles promotes filament instability, likely due to localized Joule heating and the degradation of the insulating layer at NW junctions [32,33]. Figure 3c compares the influence of polymer coating on RS. All devices show RS, with Ni@PVP$_{1:25}$ and Ni@PVP$_{1:50}$ exhibiting both volatile and nonvolatile behaviors. However, networks with the lowest PVP concentration [Ni@PVP$_{1:10}$] showed over one order of magnitude lower currents and volatile response only. Although a reduced polymer coating would be expected to increase the current due to thinner insulating layer, a previous study [34] has shown that thin switching layers in filamentary devices promote the formation of narrower conductive filaments. The smaller filament cross-section limits the current, as fewer ions are required to bridge the electrodes, resulting in lower operating currents. These results highlight the role of PVP concentration in governing ionic transport and filament formation at NW junctions.

 doi:10.20944/preprints202603.0293.v1

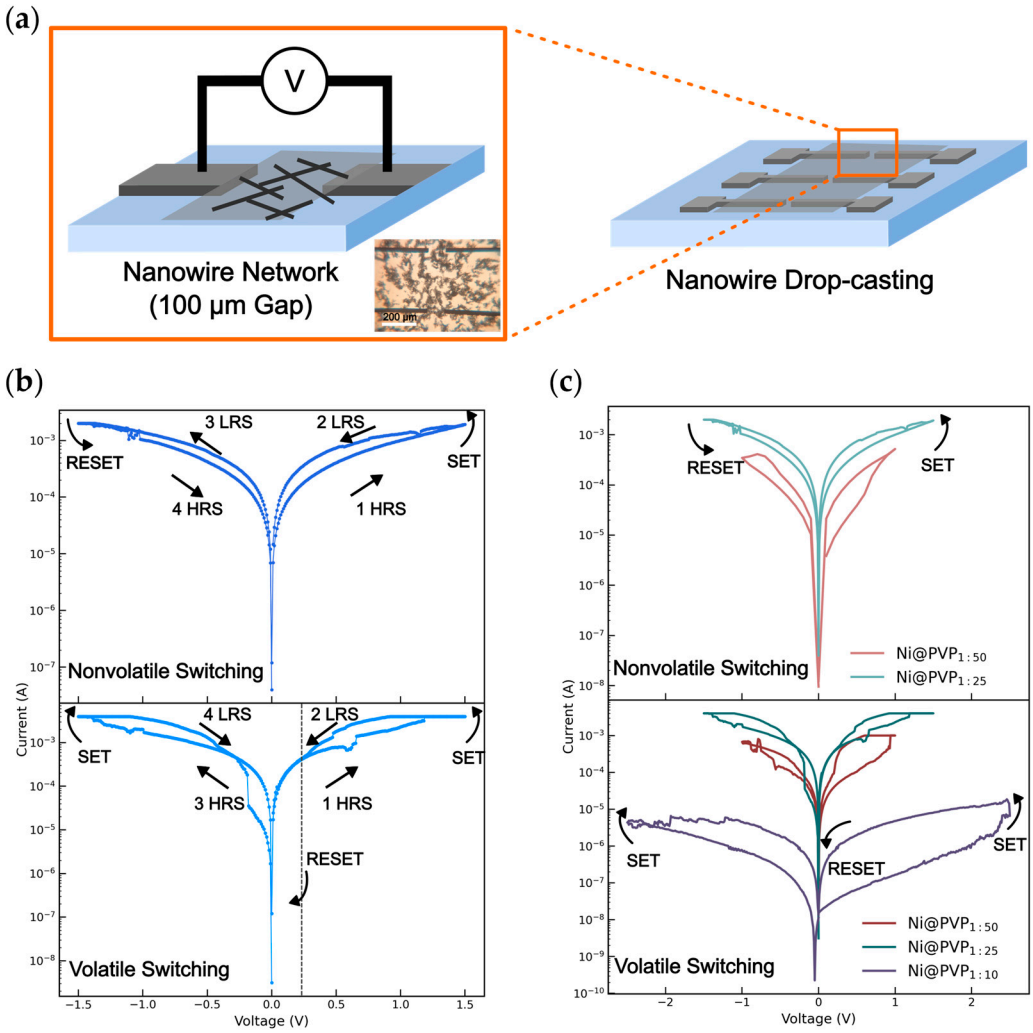

Figure 3. (**a**) Schematic of the networks. The inset shows the optical image at one of the gaps. *I–V* curves for Ni@PVP$_{1:25}$ device showing (**b**) nonvolatile and volatile RS. The grey line at 0.2 V represents the voltage where the volatile device relaxes to HRS. (**c**) Characteristic *I–V* curves for Ni@PVP nonvolatile and volatile devices with different PVP ratios of 1:10 (purple), 1:25 (green) and 1:50 (red). The arrows show the sweeping direction.

Retention was monitored for over 1 h by applying voltage read pulse of 3–5 mV under a current compliance of 0.1–1 mA (Figure 4a-c). A slight decay of the OFF resistance was observed for the Ni@PVP$_{1:10}$ device (Figure 4a). This degradation could be associated with partially irreversible ion distribution in the PVP layer [35]. Ni@PVP$_{1:10}$ devices exhibited a lower ratio (~25) and the resistance varied significantly over the 1 h measurement (Figure 4a) due to the OFF state showing large fluctuations. The Ni@PVP$_{1:50}$ devices also showed a low resistance ratio (~8.5) but comparatively smaller resistance fluctuations (Figure 4c), which could indicate that excessive PVP content increases the effective barrier thickness suppressing filament formation. In contrast, the intermediate Ni@PVP$_{1:25}$ devices exhibited the highest resistance ratio (~200) with the most stable retention over time, demonstrating an optimal polymer concentration for stable filament formation, and thus reproducible switching (Figure 4b).

 doi:10.20944/preprints202603.0293.v1

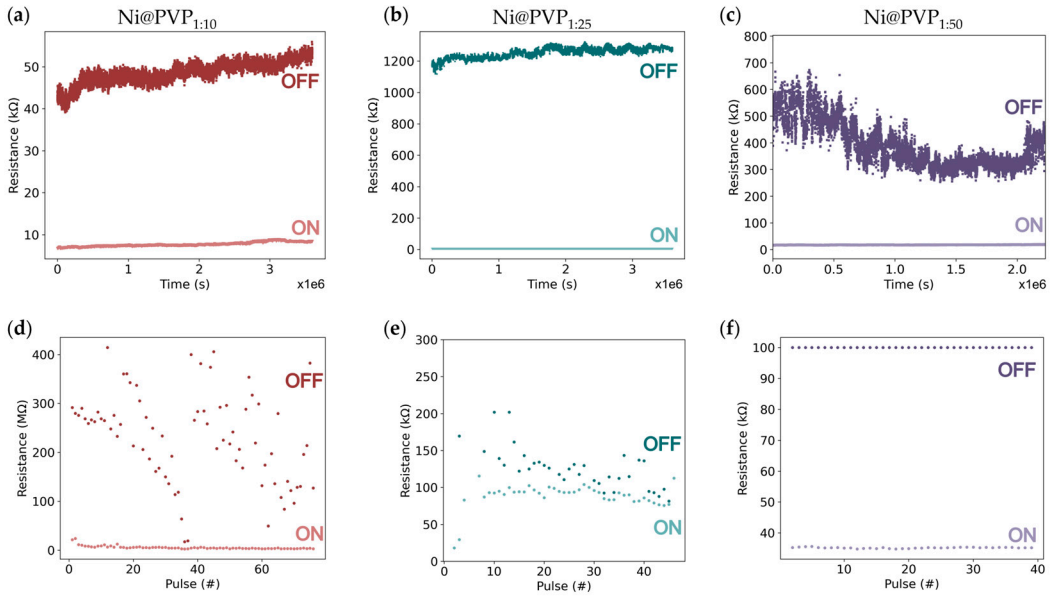

Figure 4. Retention behavior for Ni@PVP NW network devices, at a reading voltage of 3-5 mV for **(a)** Ni@PVP 1:10, **(b)** Ni@PVP 1:25, and **(c)** Ni@PVP 1:50. Endurance with pulsed voltage for **(d)** Ni@PVP 1:10 (+3 V for SET and -5 V for RESET, 100 ms width), **(e)** Ni@PVP 1:25 (+5 V for SET and -1 V for RESET, 100 ms width), and (f) Ni@PVP 1:50 (+5 V for SET and -1 V for RESET, 100 ms width).

Endurance measurements further corroborate these observations (Figure 4d-f). Ni@PVP$_{1:10}$ devices showed poor endurance performance with large current fluctuations (Figure 4d). On the other hand, both Ni@PVP$_{1:25}$ and Ni@PVP$_{1:50}$ devices exhibited stable switching, with Ni@PVP$_{1:50}$ having the most stable performance for over 50 cycles (Figure 4e and 4f, respectively). These results indicate that the switching dynamics in Ni@PVP devices are sensitive to the polymer concentration, as the polymer controls the filament length, rupture dynamics and ionic migration [10].

To investigate the dominant conduction mechanism underlaying the RS behavior, the *I–V* curves were analyzed on a log-log scale (Figure 5). During the SET of the nonvolatile network (Figure 5a), two distinct conduction regimes were observed. At low applied bias, the current increases linearly with voltage (slope ~1), indicating ohmic conduction [36,37] governed by thermally assisted carrier transport and the initial migration of metal ions through the insulating PVP layer. As the applied bias increases, the conduction transition to a space-charge-limited current (SCLC) mechanism (slopes of ~1.3 and 2), wherein injected carriers progressively fill trap states [38,39]. Once the traps are filled, a sudden increase in current occurs, corresponding to the formation of a conductive filament and the transition to the LRS (SET). In the LRS, the slope returns to ~1 at higher currents, consistent with metallic conduction. Under reverse bias (Figure 5b), the ohmic behavior is initially maintained and deviates as the voltage increases, near the RESET region (slope of 1.3–1.5), followed by an abrupt decrease in current associated with filament rupture and the return to HRS. The volatile RS follows an identical sequence of conduction mechanisms (Figure 5c and 5d), although RESET occurs before the applied voltage reaches 0 V for both positive and negative polarities. Both resistive switching behaviors are consistent with electrochemical metallization mechanisms previous reported for metal oxide and Ag-based memristive devices [19,20,22].

 doi:10.20944/preprints202603.0293.v1

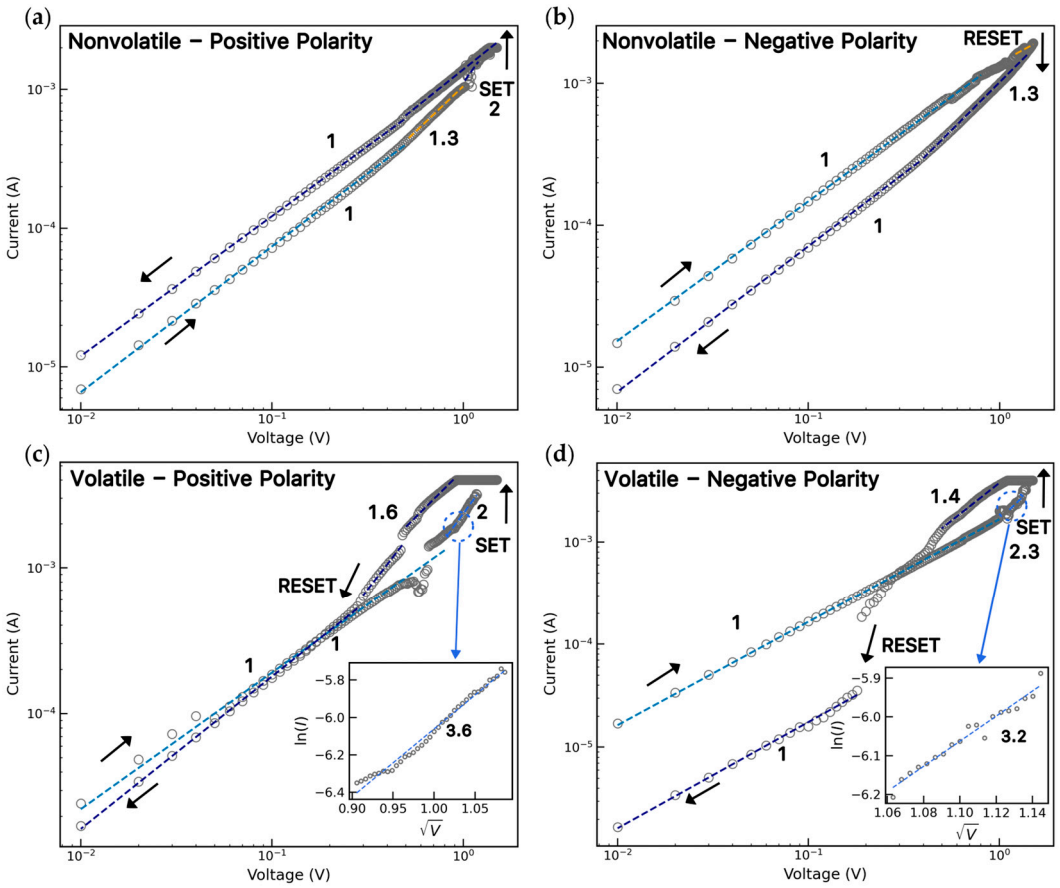

Figure 5. Log-log plots of *I–V* curves for the **(a)** SET and **(b)** RESET in nonvolatile Ni@PVP$_{1:25}$ device. **(c)** Positive and **(d)** negative polarity in volatile Ni@PVP$_{1:25}$. The insets show the plots in $ln\,(I)$ vs $\sqrt{V}$ with their respective slopes.

The prevalence of volatile RS, despite possible ion trapping in the PVP layer, shows the role of interfacial effects in these stochastic networks. Localized Joule heating at the NW junctions can induce structural changes and charge injections into the PVP layer, destabilizing the conductive filaments. In the pre-SET region of the volatile response (insets in Figure 5c and 5d), the charge transport is dominated by Schottky emission, as evidenced by the linear fit of $\ln(I)$ vs $\sqrt{V}$. This behavior is consistent with thermionic emission, where electrons gain sufficient thermal energy, facilitated by localized Joule heating at the NW junction, to pass the interfacial potential barrier of the PVP layer [40,41]. Consequently, the conductive filaments formed under bias are unstable and dissolve spontaneously upon voltage reduction, leading to the observed volatile response [41]. The transition from initial nonvolatile to dominant volatile switching likely arises from the progressive thermal modification of the junctions of the stochastic NW network over repeated cycling.

Figure 6 illustrates the RS mechanism observed in Ni@PVP NW networks inferred from electrical characterization [9,37]. RS occurs at the PVP junctions between contacting NWs, where each nickel core acts as an electrode. For volatile devices, initially, the Ni@PVP NW network is in the HRS. Under an applied bias the anodic dissolution of nickel occurs, generating nickel ions ($Ni \rightarrow Ni^{2+} + 2e^-$) which migrate through the PVP layer (Figure 6a and 6b). These ions accumulate and form a conductive filament at the junctions between nanowires, creating a percolative conduction path between the network, which leads to the SET (Figure 6c). Upon reduction or removal of the applied bias, unstable filaments may partially or fully dissolve due to ionic diffusion, resulting in relaxation back to HRS and a volatile RS (Figure 6d). The volatile nature of the switching response shapes the filament formation in the middle since it can be achieved by applying both negative and positive bias voltages [42,43].

 doi:10.20944/preprints202603.0293.v1

In contrast, nonvolatile devices exhibit thicker and more stable conductive filaments, which require reverse polarity to induce rupture. Thin coatings promote the formation of unstable filaments, whereas excessively thick coatings hinder ionic transport, leading to weak or incomplete filaments formation. Moreover, a non-uniform coating across the network may account for the observed variability, enabling the coexistent of both nonvolatile and volatile switching within the same network.

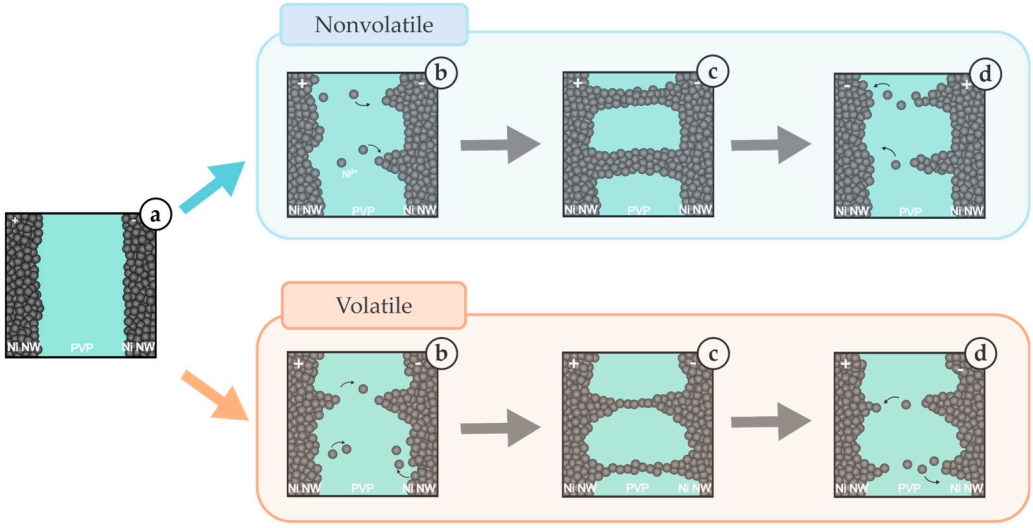

Figure 6. Schematic illustration of the filamentary RS mechanism in nonvolatile (top) and volatile (bottom) Ni@PVP NWs memristive networks. **(a)** Ni@PVP network initially in HRS, **(b)** upon increasing the applied bias, anodic dissolution of nickel creates Ni^{2+} ions that migrate through the PVP, initiating the formation of conductive filaments. (**c**) The complete formation of conductive filaments (LRS) corresponds to the SET. (**d**) By decreasing the applied bias, the filaments suffer dissolution with ions drifting back to nickel cores (HRS).

The key RS properties of the fabricated memristive NW networks are summarized and compared with those of other reported structures in Table 1. The demonstration of stable RS at 1–2 V in Ni NW networks marks a clear advance over conventional oxide-based Ni/NiO structures, which typically operate at higher voltage values (4–5 V) [19]. This low-voltage performance positions the fabricated Ni NWs devices alongside Ag-based platforms, widely recognized as the state-of-the-art in filamentary switching due to their efficient operation [16,17,22]. These devices also exhibit an R_{OFF}/R_{ON} of ~200 (for the 1:25 sample), comparable to Ag/AgO_x systems (~100) [15]. Although Ni/NiO structures can reach higher ratios (>10^5) [19], they generally rely on ordered architectures. The endurance >40 cycles, while lower than the 100–1000 cycles reported for oxide-based and Cu/TiO_2 systems [19], remains comparable to volatile Ag/AgO_x devices (~70 cycles) [15]. Furthermore, Ni provides a more sustainable and cost-effective alternative, compatible with scalable chemical fabrication routes [44,45].

Table 1. Overview of the memristive properties of NW networks for reservoirs.

 doi:10.20944/preprints202603.0293.v1

Network	Voltage (V)	Type	Retention	R_{OFF}/R_{ON}	Endurance (pulses)	Ref.
Ni@PVP$_{1:10}$	1–2	Mixed	1 h	25	40	This work
Ni@PVP$_{1:25}$				200	45	
Ni@PVP$_{1:50}$		Volatile		8.5	Poor	
Ag/Ag$_2$S atomic switches	1.5	Volatile	-	-	-	[46]
Ag/AgO$_x$	2	Volatile	-	100	35	[15]
Ti/Au/Ag/PVP planar NW network	1–8	-	-	-	-	[16]
Au/Ti/Ag/TiO$_2$ planar NW network	25–100	Volatile	-	-	40	[12]
Au/Ti/Ag/TiO$_2$ planar NW network	19	Volatile	-	-	-	[47]
Ag/ZnO mesh	4	-	-	10^5	9	[21]
Ni/Ag/PVP	20	-	-	-	-	[48]
Ni/NiO	3	-	-	>10^5	20	[13]
Ti/Au/Ni/NiO crossbar NWs	5	Nonvolatile	>24 h	10^7	10	[19]
Ti/Au/Ni/NiO mesh	5	-	-	-	10	[20]
Ti/Cu/TiO$_2$	0.6	-	-	574	100	[49]

4. Conclusions

Herein, a systematic study of stochastic memristive Ni@PVP NW networks was performed, as a cost-effective and scalable alternative to precious-metal and oxide-based memristive platforms. The synergy between the chemically stable and abundant Ni cores and the controlled polymer coating enables self-assembled NW network that operates at low voltages while maintaining competitive electrical performance. PVP coating plays a crucial role in regulating ion diffusion and filament formation, with an intermediate Ni@PVP ratio of 1:25 yielding the optimal performance. In contrast, insufficient coating (1:10) leads to unstable, predominantly volatile switching with low resistance ratios, while excessive coating (1:50) hinders ion migration and degrades switching performance. These results establish polymer thickness as a key design parameter for tuning memristive behavior in metal NW network. The Ni@PVP NW networks operate at 1–2 V, which is a significant improvement over conventional Ni/NiO-based devices (4–5 V) and comparable to state-of-the-art Ag-based platforms, with a resistance ratio of ~200, stable retention over 1 h and endurance over 45 pulses. The switching mechanism is consistent with electrochemical metallization at NW junctions, where the coexistence of volatile and nonvolatile responses reflects the stochastic variability of the network architecture. Notably, the predominant volatile switching provides intrinsic fading memory behavior which, together with the nonlinearity and high-dimensional dynamics arising from the stochastic network topology, positions Ni@PVP NW networks as promising practical platform for neuromorphic hardware applications.

Supplementary Materials: The following supporting information can be downloaded at the website of this paper posted on Preprints.org, Figure S1: Length and diameter distributions of Ni@PVP nanowires; Figure S2: SEM images of Ni@PVP NW networks at different magnifications; Figure S3: *I-V* characteristic curves of single-coated Ni@PVP.

 doi:10.20944/preprints202603.0293.v1

Author Contributions: Conceptualization, C.L., C.D., R.C. and J.V.; methodology, C.L. and R.C.; validation, C.D., R.C. and J.V.; formal analysis, C.L.; investigation, C.L.; resources, C.D., R.C. and J.V.; writing—original draft preparation, C.L.; writing—review and editing, C.L., C.D., R.C. J.V.; visualization, C.L.; supervision, C.D., R.C. and J.V.; project administration, C.D., R.C. and J.V.; funding acquisition, C.D. and J.V.. All authors have read and agreed to the published version of the manuscript.

Funding: This work was financially supported by FCT through projects LA/P/0095/2020, UIDP/04968/2025, UIDB/04968/2025, PTDC/NAN-MAT/4093/2021 and 2022.15710.UTA, and La Caixa Foundation within project CCO 204197.

Institutional Review Board Statement: Not applicable.

Data Availability Statement: The raw data supporting the conclusions of this article will be made available by the authors on request.

Conflicts of Interest: The authors declare no conflicts of interest.

Abbreviations

The following abbreviations are used in this manuscript:

HRS	High-Resistance State
LRS	Low-Resistance State
NW	Nanowire
PVP	Polyvinylpyrrolidone
RC	Reservoir Computing
RS	Resistive Switching
SE	Secondary Electrons
SEM	Scanning Electron Microscopy
XRD	X-ray Diffraction

References

1. Aguirre, F.; Sebastian, A.; Le Gallo, M.; Song, W.; Wang, T.; Yang, J.J.; Lu, W.; Chang, M.-F.; Ielmini, D.; Yang, Y.; et al. Hardware Implementation of Memristor-Based Artificial Neural Networks. *Nat. Commun.* **2024**, *15*, 1974–2014, doi:10.1038/s41467-024-45670-9.
2. Schuman, C.D.; Kulkarni, S.R.; Parsa, M.; Mitchell, J.P.; Date, P.; Kay, B. Opportunities for Neuromorphic Computing Algorithms and Applications. *Nat. Comput. Sci.* **2022**, *2*, 10–19, doi:10.1038/s43588-021-00184-y.
3. Carver Mead. Neuromorphic electronic systems. *Proceedings of the IEEE* **1990**, 1629–1636, doi:10.1109/5.58356.
4. Silva, A. V; Brandão, A.T.S.C.; Pereira, C.M.; Ventura, J.; Dias, C. Reaching Bio-Voltages and Controlling Synaptic Dynamics in Liquid-Based Neuromorphic Devices. *Nano Lett.* **2025**, *25*, 9944–9951.
5. Tanaka, G.; Yamane, T.; Héroux, J.B.; Nakane, R.; Kanazawa, N.; Takeda, S.; Numata, H.; Nakano, D.; Hirose, A. Recent Advances in Physical Reservoir Computing: A Review. *Neural Networks* **2019**, *115*, 100–123, doi:10.1016/j.neunet.2019.03.005.
6. Nakajima, K. Physical Reservoir Computing—an Introductory Perspective. *Jpn. J. Appl. Phys.* **2020**, *59*, 060501, doi:10.35848/1347-4065/ab8d4f.
7. Grácio, M.; Teixeira, H.; Dias, C.; Ventura, J. Effect of Electrode Tuning on the Resistive Switching Behaviour of MXene-Based Composites. *Polymers (Basel).* **2025**, *17*, 1309.
8. Dias, C.; Castro, D.; Aroso, M.; Ventura, J.; Aguiar, P. Memristor-Based Neuromodulation Device for Real-Time Monitoring and Adaptive Control of Neuronal Populations. *ACS Appl. Electron. Mater.* **2022**, *4*, 2380–2387.
9. Milano, G.; Porro, S.; Valov, I.; Ricciardi, C. Recent Developments and Perspectives for Memristive Devices Based on Metal Oxide Nanowires. *Adv. Electron. Mater.* **2019**, *5*, doi:10.1002/aelm.201800909.

 doi:10.20944/preprints202603.0293.v1

10. Loeffler, A.; Zhu, R.; Hochstetter, J.; Li, M.; Fu, K.; Diaz-Alvarez, A.; Nakayama, T.; Shine, J.M.; Kuncic, Z. Topological Properties of Neuromorphic Nanowire Networks. *Front. Neurosci.* **2020**, *14*, doi:10.3389/fnins.2020.00184.
11. Kuncic, Z.; Nakayama, T. Neuromorphic Nanowire Networks: Principles, Progress and Future Prospects for Neuro-Inspired Information Processing. *Adv. Phys. X* **2021**, *6*, doi:10.1080/23746149.2021.1894234.
12. Li, Q.; Diaz-Alvarez, A.; Iguchi, R.; Hochstetter, J.; Loeffler, A.; Zhu, R.; Shingaya, Y.; Kuncic, Z.; Uchida, K.; Nakayama, T. Dynamic Electrical Pathway Tuning in Neuromorphic Nanowire Networks. *Adv. Funct. Mater.* **2020**, *30*, doi:10.1002/adfm.202003679.
13. Bellew, A.T.; Bell, A.P.; McCarthy, E.K.; Fairfield, J.A.; Boland, J.J. Programmability of Nanowire Networks. *Nanoscale* **2014**, *6*, 9632–9639, doi:10.1039/C4NR02338B.
14. Manning, H.G.; Niosi, F.; da Rocha, C.G.; Bellew, A.T.; O'Callaghan, C.; Biswas, S.; Flowers, P.F.; Wiley, B.J.; Holmes, J.D.; Ferreira, M.S.; et al. Emergence of Winner-Takes-All Connectivity Paths in Random Nanowire Networks. *Nat. Commun.* **2018**, *9*, 3219, doi:10.1038/s41467-018-05517-6.
15. Du, H.; Wan, T.; Qu, B.; Cao, F.; Lin, Q.; Chen, N.; Lin, X.; Chu, D. Engineering Silver Nanowire Networks: From Transparent Electrodes to Resistive Switching Devices. *ACS Appl. Mater. Interfaces* **2017**, *9*, 20762–20770, doi:10.1021/acsami.7b04839.
16. Nirmalraj, P.N.; Bellew, A.T.; Bell, A.P.; Fairfield, J.A.; McCarthy, E.K.; O'Kelly, C.; Pereira, L.F.C.; Sorel, S.; Morosan, D.; Coleman, J.N.; et al. Manipulating Connectivity and Electrical Conductivity in Metallic Nanowire Networks. *Nano Lett.* **2012**, *12*, 5966–5971, doi:10.1021/nl303416h.
17. Milano, G.; Pedretti, G.; Montano, K.; Ricci, S.; Hashemkhani, S.; Boarino, L.; Ielmini, D.; Ricciardi, C. In Materia Reservoir Computing with a Fully Memristive Architecture Based on Self-Organizing Nanowire Networks. *Nat. Mater.* **2022**, *21*, 195–202, doi:10.1038/s41563-021-01099-9.
18. Fang, R.; Zhang, W.; Ren, K.; Zhang, P.; Xu, X.; Wang, Z.; Shang, D. In-Materio Reservoir Computing Based on Nanowire Networks: Fundamental, Progress, and Perspective. *Materials Futures* **2023**, *2*, 022701, doi:10.1088/2752-5724/accd87.
19. Ting, Y.; Chen, J.; Huang, C.; Huang, T.; Hsieh, C.; Wu, W. Observation of Resistive Switching Behavior in Crossbar Core–Shell Ni/NiO Nanowires Memristor. *Small* **2018**, *14*, doi:10.1002/smll.201703153.
20. Oliver, S.M.; Fairfield, J.A.; Bellew, A.T.; Lee, S.; Champlain, J.G.; Ruppalt, L.B.; Boland, J.J.; Vora, P.M. Quantum Point Contacts and Resistive Switching in Ni/NiO Nanowire Junctions. *Appl. Phys. Lett.* **2016**, *109*, doi:10.1063/1.4967502.
21. Puzyrev, Y.S.; Shen, X.; Zhang, C.X.; Hachtel, J.; Ni, K.; Choi, B.K.; Zhang, E.-X.; Ovchinnikov, O.; Schrimpf, R.D.; Fleetwood, D.M.; et al. Memristive Devices from ZnO Nanowire Bundles and Meshes. *Appl. Phys. Lett.* **2017**, *111*, doi:10.1063/1.5008265.
22. Milano, G.; Montano, K.; Ricciardi, C. In Materia Implementation Strategies of Physical Reservoir Computing with Memristive Nanonetworks. *J. Phys. D Appl. Phys.* **2023**, *56*, 084005, doi:10.1088/1361-6463/acb7ff.
23. Liu, P.; Li, Z.; Zhao, B.; Yadian, B.; Zhang, Y. Template-Free Synthesis of Nickel Nanowires by Magnetic Field. *Mater. Lett.* **2009**, *63*, 1650–1652, doi:10.1016/j.matlet.2009.04.031.
24. Xia, Z.; Wen, W. Synthesis of Nickel Nanowires with Tunable Characteristics. *Nanomaterials* **2016**, *6*, 19, doi:10.3390/nano6010019.
25. Staaks, D.; Olynick, D.L.; Rangelow, I.W.; Altoe, M.V.P. Polymer–Metal Coating for High Contrast SEM Cross Sections at the Deep Nanoscale. *Nanoscale* **2018**, *10*, 22884–22895, doi:10.1039/C8NR06669H.
26. Suh, I.-K.; Ohta, H.; Waseda, Y. High-Temperature Thermal Expansion of Six Metallic Elements Measured by Dilatation Method and X-Ray Diffraction. *J. Mater. Sci.* **1988**, *23*, 757–760, doi:10.1007/BF01174717.
27. Luo, M.; Hong, Y.; Yao, W.; Huang, C.; Xu, Q.; Wu, Q. Facile Removal of Polyvinylpyrrolidone (PVP) Adsorbates from Pt Alloy Nanoparticles. *J. Mater. Chem. A Mater.* **2015**, *3*, 2770–2775, doi:10.1039/C4TA05250A.
28. Li, X.-G.; Kresse, I.; Springer, J.; Nissen, J.; Yang, Y.-L. Morphology and Gas Permselectivity of Blend Membranes of Polyvinylpyridine with Ethylcellulose. *Polymer (Guildf).* **2001**, *42*, 6859–6869.

 doi:10.20944/preprints202603.0293.v1

29. Abdelrazek, E.M.; Abdelghany, A.M.; Badr, S.I.; Morsi, M.A. Structural, Optical, Morphological and Thermal Properties of PEO/PVP Blend Containing Different Concentrations of Biosynthesized Au Nanoparticles. *Journal of materials research and technology* **2018**, *7*, 419–431.
30. Mao, H.; Feng, J.; Ma, X.; Wu, C.; Zhao, X. One-Dimensional Silver Nanowires Synthesized by Self-Seeding Polyol Process. *Journal of Nanoparticle Research* **2012**, *14*, 887, doi:10.1007/s11051-012-0887-4.
31. Borodko, Y.; Habas, S.E.; Koebel, M.; Yang, P.; Frei, H.; Somorjai, G.A. Probing the Interaction of Poly (Vinylpyrrolidone) with Platinum Nanocrystals by UV- Raman and FTIR. *J. Phys. Chem. B* **2006**, *110*, 23052–23059, doi:https://doi.org/10.1021/jp063338+.
32. Uenuma, M.; Ishikawa, Y.; Uraoka, Y. Joule Heating Effect in Nonpolar and Bipolar Resistive Random Access Memory. *Appl. Phys. Lett.* **2015**, *107*.
33. Chao Yang, Y.; Pan, F.; Zeng, F. Bipolar Resistance Switching in High-Performance Cu/ZnO: Mn/Pt Nonvolatile Memories: Active Region and Influence of Joule Heating. *New J. Phys.* **2010**, *12*, 23008.
34. Zhao, H.; Dong, Z.; Tian, H.; DiMarzi, D.; Han, M.-G.; Zhang, L.; Yan, X.; Liu, F.; Shen, L.; Han, S.-J.; et al. Atomically Thin Femtojoule Memristive Device. *Advanced Materials* **2017**, *29*, 1703232.
35. Chen, Y.; Liu, G.; Wang, C.; Zhang, W.; Li, R.-W.; Wang, L. Polymer Memristor for Information Storage and Neuromorphic Applications. *Mater. Horiz.* **2014**, *1*, 489–506.
36. Wang, S.; Dong, X.; Xiong, Y.; Sha, J.; Cao, Y.; Wu, Y.; Li, W.; Yin, Y.; Wang, Y. CsFAMAPbIBr Photoelectric Memristor Based on Ion-Migration Induced Memristive Behavior. *Adv. Electron. Mater.* **2021**, *7*, 2100014.
37. Ozga, M.; Mroczynski, R.; Matus, K.; Arabasz, S.; Witkowski, B. Filamentary Resistive Switching Mechanism in CuO Thin Film-Based Memristor. *Materials* **2025**, *18*, 3820, doi:10.3390/ma18163820.
38. Zhai, S.; Gong, J.; Feng, Y.; Que, Z.; Mao, W.; He, X.; Xie, Y.; Li, X.; Chu, L. Multilevel Resistive Switching in Stable All-Inorganic n-i-p Double Perovskite Memristor. *iScience* **2023**, *26*, 106461, doi:10.1016/j.isci.2023.106461.
39. Li, D.; Ilyas, N.; Li, C.; Jiang, X.; Jiang, Y.; Li, W. Synaptic Learning and Memory Functions in SiO_2:Ag/TiO_2 Based Memristor Devices. *J. Phys. D Appl. Phys.* **2020**, *53*, 175102, doi:10.1088/1361-6463/ab70c9.
40. Deb, R.; Mallik, S.; Mishra, Y.; Padhan, R.; Sahoo, S.; Terabe, K.; Tsuruoka, T.; Mohapatra, S.R. Bias Sweep-Induced Analog Memristor Behavior, Using a Cuprous Iodide Thin Film, for Neuromorphic Computing. *ACS Appl. Electron. Mater.* **2025**, *7*, 4616–4627, doi:10.1021/acsaelm.5c00529.
41. Resende, J.; Sekkat, A.; Nguyen, V.H.; Chatin, T.; Jiménez, C.; Burriel, M.; Bellet, D.; Muñoz-Rojas, D. Planar and Transparent Memristive Devices Based on Titanium Oxide Coated Silver Nanowire Networks with Tunable Switching Voltage. *Small* **2021**, *17*, 2007344.
42. Zhao, X.; Wang, R.; Xiao, X.; Lu, C.; Wu, F.; Cao, R.; Jiang, C.; Liu, Q. Flexible Cation-Based Threshold Selector for Resistive Switching Memory Integration. *Science China Information Sciences* **2018**, *61*, 60413.
43. Shaikh, M.T.A.S.; Jeon, H.J.; Rim, Y.S. Resistive Switching Layer-Modulated Volatile and Nonvolatile Memristors with Flexible and Controlled Transient Properties. *ACS Appl. Mater. Interfaces* **2025**, *17*, 21568–21579.
44. Liu, G.-S.; Xu, Y.; Kong, Y.; Wang, L.; Wang, J.; Xie, X.; Luo, Y.; Yang, B.-R. Comprehensive Stability Improvement of Silver Nanowire Networks via Self-Assembled Mercapto Inhibitors. *ACS Appl. Mater. Interfaces* **2018**, *10*, 37699–37708.
45. Bardet, L.; Papanastasiou, D.T.; Crivello, C.; Akbari, M.; Resende, J.; Sekkat, A.; Sanchez-Velasquez, C.; Rapenne, L.; Jiménez, C.; Muñoz-Rojas, D.; et al. Silver Nanowire Networks: Ways to Enhance Their Physical Properties and Stability. *Nanomaterials* **2021**, *11*, 2785.
46. Demis, E.C.; Aguilera, R.; Scharnhorst, K.; Aono, M.; Stieg, A.Z.; Gimzewski, J.K. Nanoarchitectonic Atomic Switch Networks for Unconventional Computing. *Jpn. J. Appl. Phys.* **2016**, *55*, 1102B2, doi:10.7567/JJAP.55.1102B2.
47. Li, Q.; Diaz-Alvarez, A.; Tang, D.; Higuchi, R.; Shingaya, Y.; Nakayama, T. Sleep-Dependent Memory Consolidation in a Neuromorphic Nanowire Network. *ACS Appl. Mater. Interfaces* **2020**, *12*, 50573–50580, doi:10.1021/acsami.0c11157.
48. Fairfield, J.A.; Rocha, C.G.; O'Callaghan, C.; Ferreira, M.S.; Boland, J.J. Co-Percolation to Tune Conductive Behaviour in Dynamical Metallic Nanowire Networks. *Nanoscale* **2016**, *8*, 18516–18523, doi:10.1039/C6NR06276H.

 doi:10.20944/preprints202603.0293.v1

49. Chen, J.; Wu, Y.; Zhu, K.; Sun, F.; Guo, C.; Wu, X.; Cheng, G.; Zheng, R. Core-Shell Copper Nanowire-TiO2 Nanotube Arrays with Excellent Bipolar Resistive Switching Properties. *Electrochim. Acta* **2019**, *316*, 133–142, doi:10.1016/j.electacta.2019.05.110.